J. Fluid Mech. (1985), *vol.* 160, *pp.* 47–75
Printed in Great Britain

Influence of weak wall undulations on the structure of turbulent pipe flow: an experimental and numerical study

By M. P. CHAUVE AND R. SCHIESTEL

Institut de Mécanique Statistique de la Turbulence,
12 Avenue Général Leclerc, 13003 Marseille, France

(Received 30 May 1984 and in revised form 8 May 1985)

The influence of weak periodic wall undulations on the structure of turbulent pipe flow has been studied in three ways: measurements in air flow using pressure probes and hot-wire techniques, visualizations in water flow and numerical predictions based on a turbulence (k-ϵ) model. The flows at Reynolds numbers of 30000 and 115000 have been particularly investigated. The flow characteristics proved to be very different from those observed in a straight pipe. Calculations and experiments agree well for the mean- and turbulent-energy fields; however the detailed behaviour of some local quantities such as anisotropy of the Reynolds stress is not well predicted particularly in the crest region. So the performances and the limitations of classical closure have been appraised. The existence of an unsteady reverse-flow region downstream of every crest suggested by measurements and calculations has been clearly confirmed by visualizations in water flow.

1. Introduction

Fluid flows encountered in industry are often complex turbulent flows in the sense defined by Bradshaw, 1973. The study of these flows gives rise to numerous difficulties with respect to their experimental investigation and their numerical prediction. In recent years there has been an increased interest in the study of these complex flows, especially with a view to providing experimental data that are useful for testing and refining turbulence models. In this paper we study a fully developed turbulent flow in an axisymmetric duct with streamwise periodic wall undulations of small amplitude and a wavelength of the order of the mean duct diameter. The interest in this complex flow arises from industrial problems encountered at the C.E.A. (Commissariat à l'Energie Atomique, France) and related to turbulent heat and mass transfer. The flow presents several interacting complexities: local curvature effects near the wall; more global convergent and divergent effects periodically imposed; the existence of unsteady reverse-flow downstream of every crest; the effect of periodic sign reversal of pressure gradient, to which is eventually added the better-known effect of wall suction.

Only few experimental studies of flow in ducts with undulating walls can be found in the scientific literature. We should mention however the measurements by Hsu & Kennedy, 1971, of the flow inside of a tube with a sinusoidal wavy wall.

Nevertheless, much experimental data exists concerning various turbulent shear flows that present to a varying degree one of the complexities mentioned previously, but often in a different geometry. They can form a useful basis for comparisons and discussions. We mention for example Perry & Fairlie (1975), Eaton & Johnston (1981), Smits, Baskaran & Joubert (1981), Mueller, Korst & Chow (1964), Macagno & Tin-Kan Hung (1967) on separation and reattachment problems; Deshpande & Giddens (1980), Okwuobi & Azad (1973) on the effect of cross-sectional area variations, Kuehn (1980), Mellor (1966), McDonald (1969), on pressure-gradient effects, Hunt & Joubert (1979), So (1975), So & Mellor (1973) on curvature effects, Thorsness, Morrisroe & Hanratty (1978), Zilker, Cook & Hanratty (1977), Zilker & Hanratty (1979), on the turbulent shear flow above a surface with sinusoidal undulations.

In addition several numerical studies concerning the laminar or turbulent flow over steady or moving wavy walls have been published during the last few years (Markatos 1978; Gent & Taylor 1976; McLean 1983), and also studies concerning locally constricted pipes (Lee & Fung 1970; Oberkampf & Goh 1974).

The analysis of the properties of the turbulent flow in a wavy-walled pipe has been done in three ways: measurements in air flow; visualizations in water flow; and numerical predictions. The results have been compared with the ones obtained in classical pipe flow (Laufer 1954).

Experimental investigations carried out in air flow have been performed within a range of Reynolds numbers varying from 30000 to 115000, and these two extreme values have received particular attention.

We have determined mean-pressure and velocity fields, at six cross-sections located between two successive crests. Hot-wire velocity measurements have been extended within the viscous sublayer ($y^+ \simeq 2$), a zone of great importance for the understanding of acting dynamical mechanisms. These hot-wire measurements have been corrected for the wall-proximity effect (Chauve 1980). From the corrected measured values of velocities, we deduced the wall-shear-stress distributions. Turbulent-velocity fields have been determined using hot-wire anemometry with single-wire and cross-wire probes.

With regard to experiments in water, the existence of an unsteady reverse-flow region near the wall and downstream of every crest has been identified in photographs that give a qualitative picture of the results obtained in air and also a guide to interpreting them.

At the same time a numerical prediction of this flow has been made using a classical k-ϵ turbulence model (Jones & Launder 1972, 1973). From the application of a simple model to describe a complex flow, useful information has been inferred concerning closure hypotheses, their limitations as well as their performances.

The complexities of this flow already mentioned also present modelling problems and so the choice and the adaptation of the model are matters that require discussion. Thus the model can be a useful tool to complement and extrapolate experiments, and in particular to calculate quantities that cannot be reached by measurements.

2. Experimental set-up, procedures and experimental conditions

2.1. *Description of experimental model*

An experimental model with a porous wall was designed at the C.E.A. and constructed using fritted bronze. An axial cross-section (figure 1) shows the basic undulation shape. The entire model comprises nine such adjoining shapes. The tube thickness varies periodically but its external diameter remains constant. The tube is 495 mm long and was built in three parts, each comprising three undulations. The

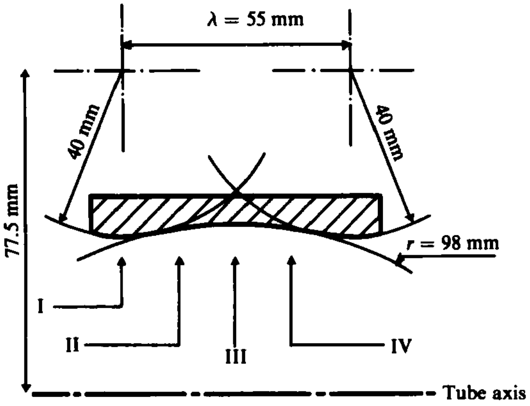

FIGURE 1. Sketch of an undulation shape.

mean precision of the whole setting is about 1 mm on the diameter, a value that can be taken as satisfactory considering manufacturing difficulties.

The manufacturing process was carried out in three stages: metal casting, pressing and soldering during assembly. The material used is a fine bronze powder made of calibrated spherical particles of diameter $d = 0.05$ mm. The core of the mould is made of a special steel plate which was machined and ground according to the desired profile. Fritting of the bronze powder was obtained by firing in an oven. Every plate is shaped by pressing in order to give a half-shell. The forge-hammer tip was also shaped according to previously defined undulations of 2.8 mm amplitude. To achieve a definitive shape required numerous strikings. Two half-shells 165 mm long are joined by soft soldering to make a cylindrical stump (composed of three elementary undulations), then three of these stumps are fitted together, also by soldering, to make a porous tube 495 mm long. The three stumps were aligned during soldering using a chuck placed inside the tube. For the present experimental conditions, we checked that the tube could be considered as hydrodynamically smooth: we found that Reynolds number $U_{*\mathrm{H}}d/\nu$ based on the diameter d of the bronze particles and on the nominal friction velocity $U_{*\mathrm{H}}$ did not exceed 32; it is therefore smaller than the usual limiting value of 70 (Brun, Martinot-Lagarde & Mathieu 1968).

2.2. *The aerodynamic wind tunnel*

The porous tube is separately located in a suction-box which is connected to an aspirator. The whole apparatus is attached to the exit of a blower-type wind tunnel with horizontal axis (Verdier 1977). The experimental model under examination is preceded by an airtight inlet manifold of 75 mm interior diameter and 4 m long, to allow the turbulent flow to become fully developed within approximately 50 diameters. The link between this manifold and the porous tube is made with a bronze thimble. This thimble includes two diametrically opposite wall pressure probes and allows, through rotation, a check on the axisymmetry by measuring the pressure in several diameter positions. The link between experimental model and bronze thimble occurs at a crest. The model length has been fixed at 450 mm, i.e. a little more than eight undulations. A schematic diagram of the installation is shown in figure 2. The mean-flow rate at the inlet is controlled by measuring the head loss over a reference length in the airtight manifold, taking into account temperature and atmospheric pressure variations. Symmetry of mean-velocity profiles was checked along two orthogonal diameters.

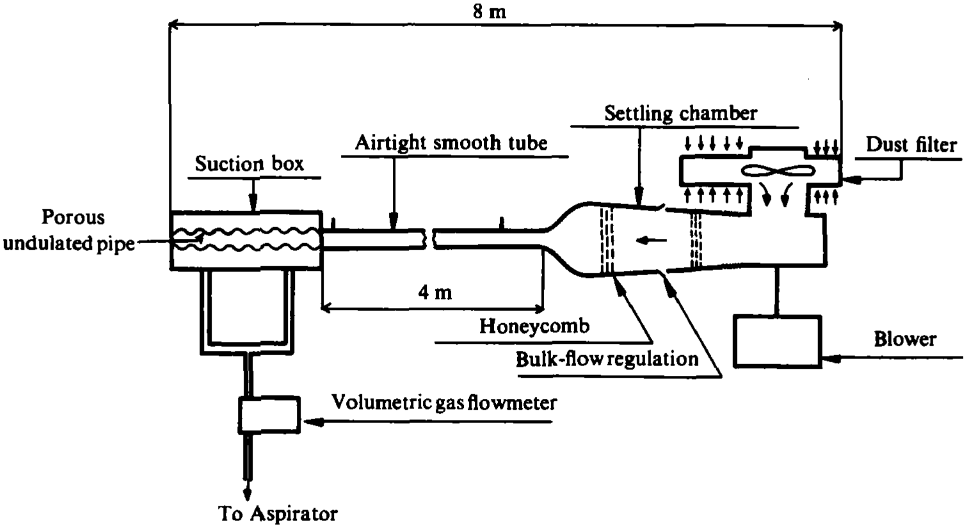

FIGURE 2. Schematic diagram of the flow system.

2.3. *Probes and equipment*

A traversing mechanism is used to move probes in three directions: the longitudinal direction parallel to the axis of the model with a 0.5 mm precision, the horizontal direction in the cross-section with a 0.1 mm precision, and the vertical direction with a 0.1 mm precision. The use of 'X-wire' probes required, in addition to the previous mechanism one which allowed rotations about two axis perpendicular to the planes of symmetry of the 'X-wire' probes.

The pressure probes are classical Pitot tubes connected to water micromanometers. Hot-wire probes are made in the laboratory; they are designed to allow measurements within the viscous sublayer. The probe pins make a 50° angle to the wall, and are of length about 20 mm and tip diameter 0.1 mm. Wires are made of rhodium-plated tungsten, of length 1.6 mm and diameter 5 µm. DISA X-probes were altered to minimize spacial integration effects. Specifically, the spacing between wires' planes was reduced to 0.4 mm as in a previous study (Fulachier 1972). The wire diameter is 5 µm and the wire length is about 1 mm. The model axis is located by inserting a cylindrical bar inside the undulated tube: the length of this bar corresponds to four undulation lengths and its diameter equals the model diameter at the crests. Every probe is located relative to this reference axis. In addition, the determination of single-wire probes position near the wall is controlled by an electrical contact visualized on the screen of an oscillograph. Distances from the wall are measured using a dial-micrometer giving a $\frac{1}{100}$ mm precision.

In order to detect flow reversal a special two-wire probe was built (Chauve 1981). The sensor is composed of a platinum wire of diameter 1 µm acting as a resistance thermometer located upstream and by a classical hot wire of diameter 5 µm. The distance between the two wires is 0.2 mm. The upstream 'cold' wire is operated with a constant-current circuit. The other wire is connected to a constant-temperature anemometer at an overheat of 0.8. When flow reversal occurs, the upstream wire detects the thermal wake coming from the hot wire located upstream, as shown in figure 3. A similar arrangement to detect flow reversal in the outer part of a jet into still air was used by Antonia, Chambers & Hussain (1980).

Hot-wire measurements are made with a constant-temperature anemometer (DISA

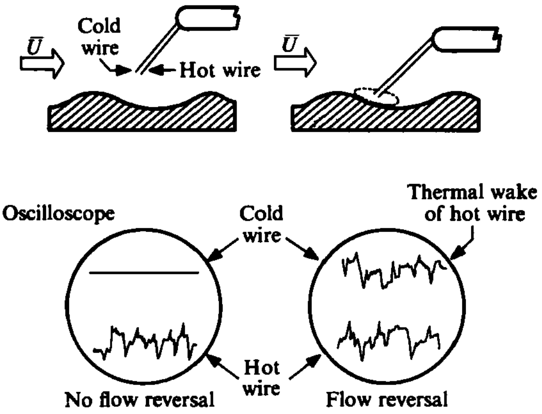

FIGURE 3. Detector of flow reversal.

55M01), a linearizer (DISA 55D10), and an auxiliary unit (DISA 55D25); a correlator (DISA 55D70) is also used for 'X-wire' measurements.

Calibration of probes is carried out on the axis of the undulated tube, straight tube of circular cross-section having been placed inside the model in order to suppress any influence from the undulations.

The axial mean velocity was measured with a Pitot tube connected to a differential water micromanometer. For all these measurements, the influence of temperature and atmospheric-pressure variations was taken into account.

2.4. *Wall friction*

The presence of undulations at the wall places severe constraints on the experimental determination of the wall shear stress. We know that the stress is related to the mean-velocity gradient in the viscous sublayer by the relationship: $\tau = -\mu \partial U/\partial y$ where y is the distance from the wall. Then, a 'natural' method for determining the shear stress consists in directly measuring the mean velocity inside the sublayer with a hot wire. Unfortunately, the sublayer thickness is, in most cases, very small. Within these distances (< 1 mm) the hot wire undergoes extra cooling from the wall which must be taken into account, and so a special study was conducted in a smooth tube to yield the corrections that have to be applied in such experimental conditions (Chauve 1980). Probe calibration at different distances y from the wall allowed the determination of the coefficients A and B that appear in the usual calibration relation ($E^2 = A + BU^n$) where n is assumed constant. The mean velocity $\bar{U}$ in the undulated model was obtained, at each distance, from the values of A and B corrected for wall proximity. Moreover, and because of wall curvature, the probe does not move exactly along the normal but we have verified (Chauve 1981) that errors thus introduced in the determination of τ_p were negligible ($< 4\,\%$) in comparison with the accuracy of measurements.

2.5. *Experimental conditions*

To define reference quantities we consider a cylindrical duct of circular cross-section, displaying the same lateral area S_λ along one wavelength λ and conveying the same flow rate as the undulated tube. Then we define the following quantities:

mean radius	$a_H = S_\lambda/2\pi\lambda$;	$(a_H = 39.3 \text{ mm})$
mean bulk velocity	$\tilde{u}_H = Q_H/\pi a_H^2$;	
mean Reynolds number	$Re_H = 2\tilde{u}_H a_H/\nu$.	

The overall friction factor is obtained from Blasius formula: $\Lambda_{*\mathrm{H}} = 0.316\, Re_{\mathrm{H}}^{-\frac{1}{4}}$ from which we deduce:

mean wall shear stress $\tau_{\mathrm{H}} = \frac{1}{8}\rho\tilde{u}_{\mathrm{H}}^{2}\ \Lambda_{*\mathrm{H}}$ and
mean friction velocity $U_{*\mathrm{H}} = (\tau_{\mathrm{H}}/\rho)^{\frac{1}{2}}$.

Two different flow rates have been considered, corresponding to $\tilde{u}_{\mathrm{H}} = 5.7$ m/s and $\tilde{u}_{\mathrm{H}} = 21.9$ m/s that is to say $Re_{\mathrm{H}} = 30000$ and $Re_{\mathrm{H}} = 115000$. Wall-suction rates are defined by the ratio $A = v_{\mathrm{P}}/\tilde{u}_{\mathrm{H}}$ where v_{P} is the suction velocity at the wall deduced from measurement of the aspired flow rate.

For the suction experiments, the head loss in the airtight tube is restored to the same value as in experiments without suction, in order to maintain a constant inlet flow rate. Suction rates vary from 0 to 50.10^{-4} at most.

2.6. *Visualizations*

In order to perform the visualizations, an exact copy of the model used for the experimental study in air was built in Plexiglas, and set up as a branch of the hydrodynamic tunnel at IMST which works continuously driven by gravity. Between the 4th and 5th crests, nine equidistant injectors were placed at the wall in order to visualize particularly this region of the flow. The injected dye is fluorescein. Light is introduced in thin luminous sheets (a few millimetres thick). Instantaneous photographs were taken using a 120 Joules electronic flash with exposures of order 1 ms.

3. Numerical approach

3.1. *Choice of mathematical model of turbulence*

This is a ticklish choice that demands a compromise. Although it may be claimed that turbulence models using one-point closures have led to the development of efficient prediction methods for turbulent shear flows in simple geometries such as boundary layers, free jets and flow in straight pipes, this is not the case for complex flows. These latter flows throw up many unsolved problems in turbulence modelling. These problems have several different sources.

For instance, Bradshaw (1973) showed in particular that an extra strain rate superimposed on the flow has an effect of unexpected magnitude on the flow structure. Very often, this effect is an order of magnitude higher than would be expected from the only additional explicit terms in the equations. Taking into account such an effect in numerical modelling is a difficult task.

Also, we know that turbulent flows in complex geometries promote the development of 'coherent structures' which are clearly revealed in flow visualization and play an important dynamic role. Again, in this case, we don't know how to make the appropriate modifications in the models.

Indeed there remain many other turbulence-modelling problems of a phenomenological kind. For instance, problems concerning the intermittency near free boundaries or small-scale intermittency, or those related to the history of turbulence.

Under such conditions we did not try, within the scope of this study, to include improvements in modelling that would be specific to the present study but which would not have general implications. Our aim is rather to try to assess the performance of a widely accepted classical closure for the case of a complex turbulent shear flow. The k-ϵ model of Jones & Launder (1972) seemed to us to meet these requirements. Indeed, this model has been widely used for calculation of turbulent shear flows, allowing the closure hypothesis to be substantiated in an extensive field of applications. In general, it yields a good compromise between precision and universality, between performance and tractability. Of course, the model also allows calculation of additional quantities that would be difficult to measure, such as the turbulent-energy dissipation rate or energy balance, and so it complements experimental investigations.

In the case of the tube with an undulated wall we have applied the low-Reynolds-number version of the k-ϵ model (Jones & Launder 1972, 1973) in order to describe completely the viscous sublayer adjacent to the wall which plays such an important part in the flow dynamics. This method prevents the use of any wall function to specify boundary conditions. In the present situation, the pressure gradient varies strongly along an undulation and the flow does not respond instantaneously to its variations. A lag is expected to appear between the local pressure gradient and the flow response. To allow for this it has been demonstrated by Hanratty, Abrams & Frederick (1983) that inclusion of some relaxation mechanism is of central importance. The k-ϵ model in which the relaxation phenomenon is inherent to the transport equations of k and ϵ, seems to be better suited to this case than any algebraic model based on turbulent viscosity. Moreover, we have tried to introduce the effect of periodic curvature of the wall by taking numerical coefficients of the model as functions of a curvature parameter according to a modification proposed by Launder (1975).

3.2. *Analytical description of the undulated wall*

We use a curvilinear mesh fitted to the shape of the undulations at the wall (Schiestel 1979), in order to describe carefully the viscous region adjacent to the wall where large gradients of turbulent quantities prevail. This choice also facilitates the introduction of wall boundary conditions. The curvilinear net has been obtained by a conformal mapping defined by analytic functions. The methodology is very similar to that used by Gent & Taylor, (1976) and Taylor, Gent & Keen (1976) also based on conformal mapping, but for a somewhat different shape of undulation.

One can briefly sum up the steps of the procedure in the following way. We first note that the analytic function $\zeta = f(\eta)$ which maps the exterior of a circle onto the exterior of a closed contour can be developed as series of η of the form:

$$\zeta = \sum_{m=-1}^{+\infty} \alpha_m \eta^m.$$

The corresponding transformation is then composed right and left by the elementary transformations

$$\zeta = \mathrm{e}^{-\mathrm{i}\mathbb{K}Z}, \quad \eta = \mathrm{e}^{\mathrm{i}\mathbb{K}z} \quad \text{with} \quad \mathbb{K} = 2\pi a_{\mathrm{H}}/\lambda,\ \mathrm{i}^2 = -1.$$

The resulting global transformation can be written (figure 4*a*):

$$Z = z + \frac{\mathrm{i}}{\mathbb{K}} \ln Q(\mathrm{e}^{\mathrm{i}\mathbb{K}z}),$$

where Q is defined by

$$Q(\eta) = \sum_{m \geqslant 0} \alpha_{m-1} \eta^m.$$

This analytic function allows the half-plane $y \geqslant 0$ to be mapped onto the half-plane above the periodic boundary.

The shape of the boundary curve is defined in parametric form by $Z = t + \mathrm{i}S(t)$ (or

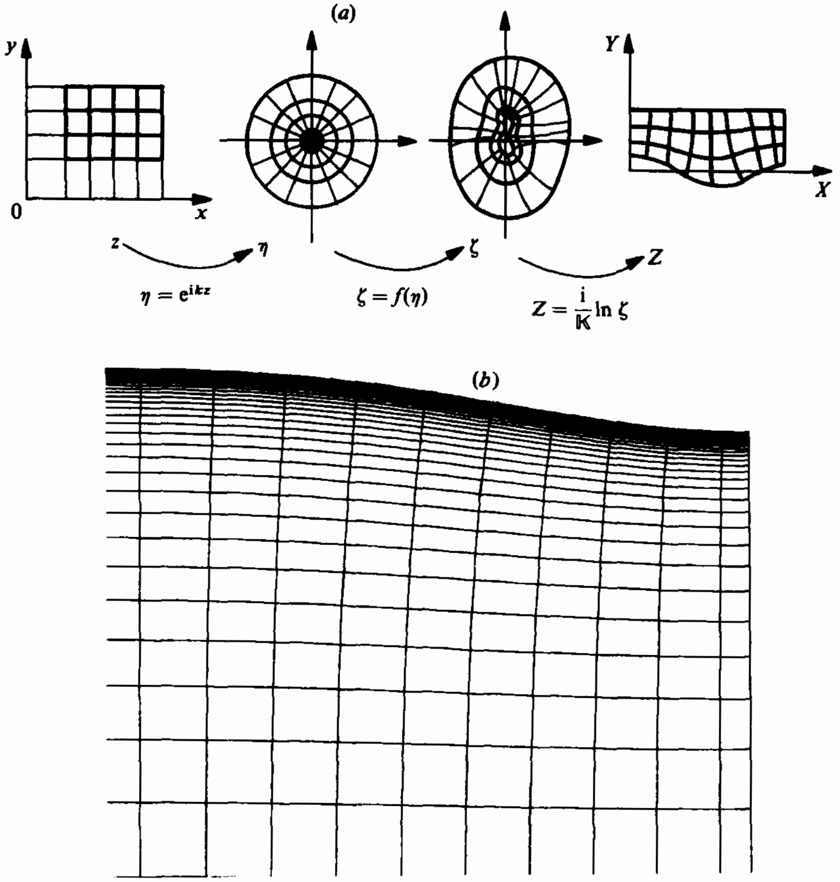

FIGURE 4. (*a*) Sketch of successive transformations. (*b*) Computational curvilinear grid.

by $\zeta = e^{s(t)-it}$). The method of Kantorovich & Krylov (1964) allows the determination of the change in variables $t = t(\eta)$ such that the function $\zeta(\eta) = \zeta[t(\eta)]$ is holomorphic.

We find to a first-order approximation that

$$Z = z + \frac{i}{\mathbb{K}} \ln\,(a_0 + a_1\,e^{i\mathbb{K}z} + a_2\,e^{2i\mathbb{K}z}).$$

This transformation acts on an infinite half-plane, but in fact the interval in the present problem remains finite. So, in order to reduce residual undulations on the tube axis, an extra term has been added:

$$Z = z + \frac{i}{\mathbb{K}} \ln\,(a_{-1}\,e^{-i\mathbb{K}z} + a_0 + a_1\,e^{i\mathbb{K}z} + a_2\,e^{2i\mathbb{K}z}).$$

The following coefficient values have been used:

$$a_0 = 0.9905, \quad a_1 = 0.1589, \quad a_2 = 0.0220, \quad a_{-1} = -a_1\,e^{-2\mathbb{K}}.$$

The boundary curve thus obtained approximates the shape of the undulated wall with a precision of 0.2 % of tube radius (i.e. 1.5 % of the amplitude of undulations), an accuracy which is distinctly superior to concrete model realization (figure 4*b*). The residual undulations on the tube axis are entirely negligible.

3.3. *Governing equations*

Equations of motion for the mean flow and turbulence transport equations have been written in curvilinear orthogonal coordinate systems. They are as follows:

momentum equations

$$\nabla(1)\, U_1^2 + \nabla(2)\, U_1\, U_2 - J(1)\, U_2^2 + J(2)\, U_1\, U_2$$
$$= \frac{1}{\rho}\frac{\partial p}{\partial y(1)} - \nabla(1)\, R_{11} - \nabla(2)\, R_{12} + J(1)\, R_{22} - J(2)\, R_{12} + H(1)\, R_{33};$$

$$\nabla(1)\, U_1\, U_2 + \nabla(2)\, U_2^2 + J(1)\, U_1\, U_2 - J(2)\, U_1^2$$
$$= -\frac{1}{\rho}\frac{\partial p}{\partial y(2)} - \nabla(1)\, R_{12} - \nabla(2)\, R_{22} + J(2)\, R_{11} - J(1)\, R_{12} + H(2)\, R_{33};$$

continuity

$$\nabla(1)\, U_1 + \nabla(2)\, U_2 = 0;$$

turbulent-kinetic-energy equation

$$\nabla(1)\,(kU_1) + \nabla(2)\,(kU_2) = \mathscr{P} - \epsilon + \nabla(1)\left(\sigma_k \frac{\partial k}{\partial y(1)}\right) + \nabla(2)\left(\sigma_k \frac{\partial k}{\partial y(2)}\right),$$

with

$$\sigma_k = \nu + \nu_{\mathrm{t}};$$

turbulent kinetic-energy dissipation-rate equation

$$\nabla(1)\,(U_1\,\tilde{\epsilon}) + \nabla(2)\,(U_2\,\tilde{\epsilon}) = C_{1\epsilon}\frac{\tilde{\epsilon}}{k}\mathscr{P} - C_{2\epsilon} f_\epsilon \frac{\tilde{\epsilon}^2}{k} + C'_{1\epsilon}\,\nu\nu_t\left[\left(\frac{\partial^2 U_1}{\partial y(2)\,\partial y(2)}\right)^2 + \left(H(2)\frac{\partial U_1}{\partial y(2)}\right)^2\right]$$
$$+ \nabla(1)\left(\sigma_\epsilon \frac{\partial \tilde{\epsilon}}{\partial y(1)}\right) + \nabla(2)\left(\sigma_\epsilon \frac{\partial \tilde{\epsilon}}{\partial y(2)}\right),$$

with

$$\sigma_\epsilon = \nu + \frac{\nu_t}{1.3}, \quad C_{1\epsilon} = 1.44, \quad C_{2\epsilon} = 1.92, \quad C'_{1\epsilon} = 2.0;$$

auxiliary relations

$$\nu_t = C_\mu\, k^2/\epsilon,$$

with

$$C_\mu = 0.09 \exp\left[\frac{-3.4}{(1 + Re_{\mathrm{T}}/50)^2}\right],$$

$$R_{11} = \tfrac{2}{3}k - 2\nu_{\mathrm{t}}\left(\frac{\partial U_1}{\partial y(1)} + U_2\, J(2)\right),$$

$$R_{22} = \tfrac{2}{3}k - 2\nu_{\mathrm{t}}\left(\frac{\partial U_2}{\partial y(2)} + U_1 J(1)\right),$$

$$R_{33} = \tfrac{2}{3}k - 2\nu_{\mathrm{t}}(H(1)\, U_1 + H(2)\, U_2)$$

$$R_{12} = -\nu_t\left(\frac{\partial U_1}{\partial y(2)} + \frac{\partial U_2}{\partial y(1)} - U_1\, J(2) - U_2\, J(1)\right),$$

$$\mathscr{P} = -R_{ij}\frac{\partial U_i}{\partial y(j)} - U_1(R_{22}\, J(1) - R_{12}\, J(2)) - U_2(R_{11}\, J(2) - R_{12}\, J(1)),$$

$$\epsilon = \tilde{\epsilon} + \frac{\nu}{2k}\frac{\partial k}{\partial y(2)}\frac{\partial k}{\partial y(2)},$$

$$f_\epsilon = 1 - 0.3 \exp\left(-Re_{\mathrm{T}}^2\right), \quad Re_{\mathrm{T}} = \frac{k^2}{\nu\tilde{\epsilon}};$$

geometrical relations

$$J(j) = \frac{1}{2J}\frac{\partial J}{\partial y(j)}, \quad H(j) = \frac{1}{r}\frac{\partial r}{\partial y(j)}, \quad j = 1, 2.$$

Each of the transport equations can be written in the general form

$$\nabla(1)\left[U_1\phi - \sigma_\phi \frac{\partial \phi}{\partial y(1)}\right] + \nabla(2)\left[U_2\phi - \sigma_\phi \frac{\partial \phi}{\partial y(2)}\right] = S_\phi,$$

where

$$\nabla(j)\phi = \frac{1}{rJ^{\frac{1}{2}}}\frac{\partial(rJ^{\frac{1}{2}}\phi)}{\partial y(j)} \quad \text{(derivation operator)},$$

$$\mathrm{d}y(j) = J^{\frac{1}{2}}\,\mathrm{d}y_j \quad \text{(infinitesimal length element)},$$

$$J = \left|\frac{\mathrm{D}(Y_1, Y_2)}{\mathrm{D}(y_1, y_2)}\right|, \quad j = 1, 2 \quad \text{(Jacobian determinant)},$$

with

$$Z = Y_1 + \mathrm{i}\,Y_2, \quad z = y_1 + \mathrm{i}y_2.$$

It is well known that longitudinal curvature may have a large influence on turbulent flows.

Noting that the production rate of turbulent kinetic energy can be approximated by

$$\mathscr{P} \approx -R_{12}\frac{\partial U_1}{\partial y(2)}\left(1 - \frac{U_1 J(2)}{\partial U_1/\partial y(2)}\right),$$

where the curvature parameter is

$$S = \frac{U_1 J(2)}{\partial U_1/\partial y(2)},$$

$J(2)$ represents the longitudinal curvature of the curvilinear coordinate system, and is usually close to the streamline curvature.

According to Bradshaw (1969) we introduce the Richardson number:

$$Ri = 2S(1+S) = \frac{2U_1 J(2)}{(\partial U_1/\partial y(2))^2}\frac{1}{J^{\frac{1}{2}}}\frac{\partial(J^{\frac{1}{2}}U_1)}{\partial y(2)}.$$

Launder (1975) suggested that the characteristic time $(\partial U_1/\partial y(2))^{-1}$ be replaced by k/ϵ, which is of a similar order of magnitude. He also suggested the use of a modified Richardson number

$$Ri' = \frac{U_1 J(2)\,k^2}{\epsilon^2 J^{\frac{1}{2}}}\frac{\partial(J^{\frac{1}{2}}U_1)}{\partial y(2)}.$$

The $C_{2\epsilon}$ coefficient in the transport equation for ϵ is then replaced by $C_{2\epsilon}\,(1 - 0.25\,Ri')$. Numerical calculations have been carried out with and without this modification in order to assess its importance.

3.4. *Numerical resolution*

The motion equations have been solved in primitive variables. Shifted grids (figure 5) have been introduced for the calculation of velocity components (Amsden & Harlow 1970).

The basic net of discretization points presents 22 points in the longitudinal direction and 40 points along a radius; the mesh is contracted near the wall such that the ratio between two contiguous steps in space is constant and equal to 0.8.

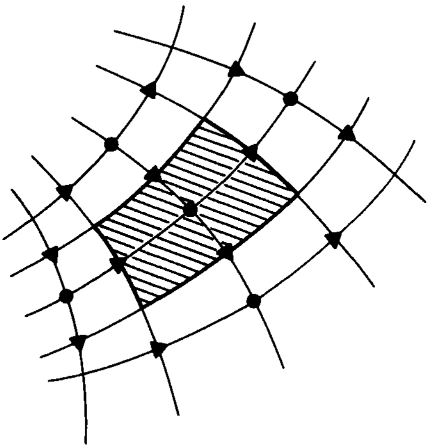

FIG. 5. Discretization cell.

Discretized equations are obtained in the transformed plane by the finite-volume approach. This method consists of an integration of the differential equations in the cell volume surrounding a net point (Patankar 1980; Gosman, Khalil & Whitelaw 1977). Convection terms are approximated using an upwind scheme. This scheme introduces an artificial viscosity ν_{false} which has been estimated by De Vahl Davis & Mallison, quoted in Patankar (1980). We notice that in the core region, the velocity vectors are almost aligned with coordinate lines. Near the recirculating zone (figure 12) the velocities become weak and in this critical region we found that the ratio ν_{false}/ν_t remained below 8%. The solution algorithm is developed on the basis of the calculation procedure of Pun & Spalding (1977) for elliptic flows with weak recirculation. The discretized equations, written in a linearized form, are solved by iterations using a line-by-line procedure. The solution for each variable on a cross-stream section is performed before advancing the sweep (NEAT arrangement, Pun & Spalding 1977). Cell-wise continuity is enforced by solving a pressure-correction equation but is also preceded by a strip-wise adjustment of overall continuity enforcing the fixed flow rate in a cross-section, with consequent pressure changes over the remainder of the field. This method of Pun & Spalding has been adapted to curvilinear geometry. Calculations are run, undulation after undulation, from the inlet down to the fourth crest. Boundary conditions at the inlet are given by steady profiles in a straight tube obtained numerically using the same turbulence model (Schiestel & Chauve 1982). For subsequent undulations, upstream boundary conditions are given by the solution already obtained at the exit of the previous undulation. Exit boundary conditions for every undulation assume zero second derivatives for each calculated function at a crest, where there is no recirculation. Boundary conditions, at the wall specify vanishing of the quantities U_1, U_2, k, and $\tilde{\epsilon}$.

Owing to the nonlinearity and the coupling of the equations, a combination of underrelaxation and linearization of source terms is necessary to ensure convergence of the overall procedure. Convergence is controlled through residual-sources evolution and settling of calculated values at preselected nodes.

4. Experimental and numerical results

4.1. *The mean fields*

4.1.1. *Mean-pressure field*

Variations of the overall friction factor $\Lambda_* = 4a_H \Delta p/\lambda\rho\tilde{u}_H^2$ are shown in figure 6 as a function of Reynolds number Re_H. There is an important increase in Λ_* due to the presence of undulations. In the undulated pipe, these variations are well correlated by the following empirical relation: $\Lambda_* = 37.9\, Re_H^{-0.62}$. This relation departs from the classical Blasius formula over the range, decreasing with increasing Reynolds numbers. Good agreement between experiments and calculations is found at a Reynolds number of 115000.

In the presence of wall suction and for suction rates varying from 0 to 20.10^{-4} the resulting increase in head loss approaches the value obtained in circular straight pipes at higher Reynolds numbers (table 1), (Verdier 1977; Elena 1977). Thus for $Re_H = 110000$ we corroborate the results given by Verdier.

Radial variations of pressure, relative to its value on the axis, are shown in figure 7 (*a*, *b*) at four sections between two successive crests. They indicate a minimum value at the crest and a maximum value in the trough. Sign changes in $\varphi(r)$ follow roughly the changes in wall curvature. However, at a Reynolds number of 30000, a change of sign occurs upstream of section II because of the existence of unsteady reverse flow. At a Reynolds number of 115000 numerical predictions are in good agreement with experimental results. At 30000, in spite of poorer agreement, we note that at section II $\varphi(r)$ is still negative, revealing the previously noted lag.

If we now consider the longitudinal evolution of the mean pressure, plotted in figure 8, we observe the presence of a phase shift between pressure-distribution curves and wall undulations. This is strongly pronounced at a Reynolds number of 30000 and is practically non-existent at 115000. This result is again noticeable, although much weaker, on calculated curves. Flow reversal would explain the phase shift observed at low velocities. An increase in the Reynolds number results in a more symmetrical longitudinal distribution, reflecting the extreme situation of a perfect fluid (Verdier 1977).

Calculated pressure contours, plotted on figure 9, supported the preceding remarks: in particular, we note that contour curves for the two Reynolds numbers coincide in the convergent region while there is significant deviation in the divergent region where reverse flow occurs.

4.1.2. *Mean-velocity field*

Experimental and calculated profiles of mean velocity are presented in figures 10 (*a*)–(*d*) for 4 sections, the first being located at the 4th crest and the others regularly spaced within one undulation at two Reynolds numbers $Re_H = 30000$ and 115000. These profiles are plotted in semi-logarithmic form, values are normalized with constant friction velocity U_{*H} equal to that in a straight tube at the same Reynolds numbers as defined in §2.5. The universal logarithmic law has been drawn for comparison.

At section I, measured and calculated profiles are distinctly different from the universal profile. In fact, the existence of a strong shear stress at the crest implies upward-shifted profiles lying above the universal profile, particularly for low values of y^+. At section II, a region where the wall shear stress is very weak, profiles are shifted downward, below the universal profile. Half-way between two crests, at

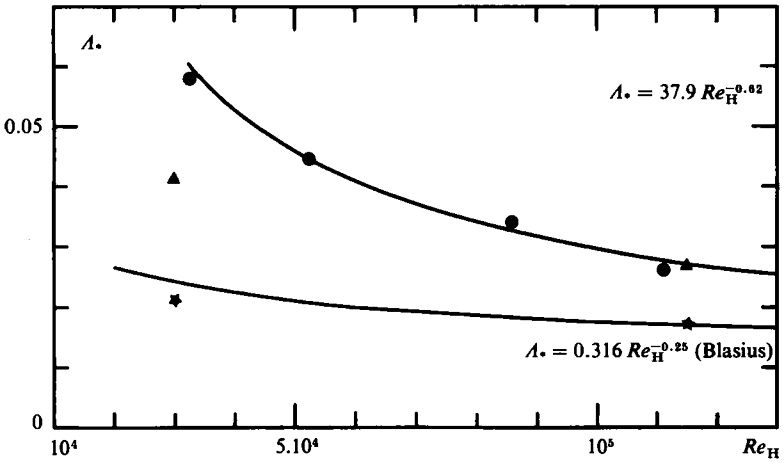

Figure 6. Overall friction factor *versus* Reynolds number: ●, experiments; ▲, undulated-pipe calculation; ★, straight pipe calculation.

		Undulated tube			Smooth tube
	$10^3\,Re_H$	30	50	110	$19 \leqslant 140$
$10^3 A$	1.0	0.0284	0.0216	0.0144	0.0132
	2.0	0.0444	0.0356	0.0268	0.0258

Table 1. Values of $(\Lambda_*)_{A=0} - (\Lambda_*)_{A \neq 0}$.

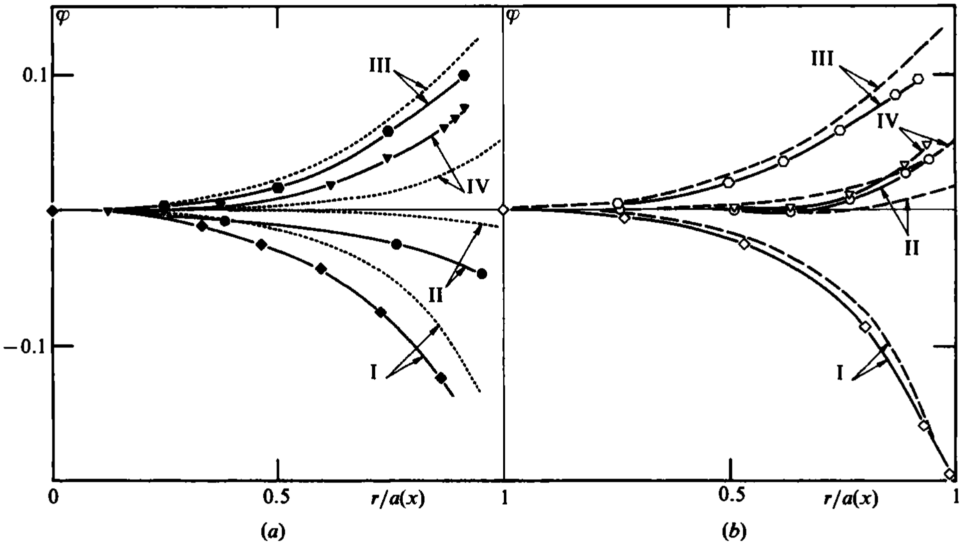

Figure 7. Radial distribution of pressure $\varphi = 2(p(r) - p(0))/\rho \bar{U}_H^2$. (*a*) $Re_H = 30000$ (——, experiments; ......, calculation). (*b*) $Re_H = 115000$ (——, experiments; ----, calculation).

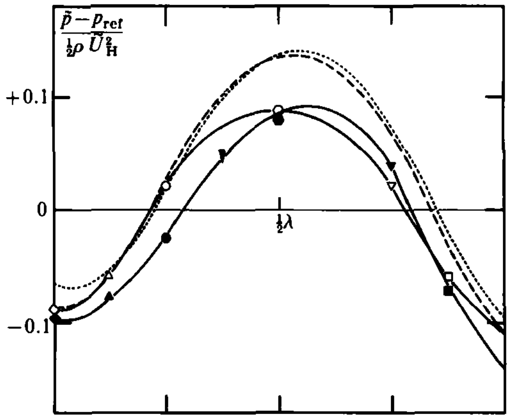

FIGURE 8. Longitudinal mean-pressure distribution, $Re_H = 30000$ (◆——■, experiments; ......, calculation), $Re_H = 115000$ (◇——□, experiments; ...., calculation).

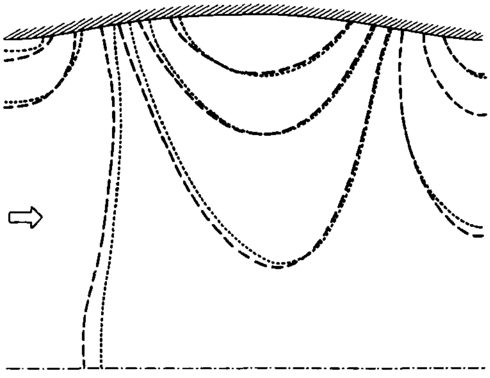

FIGURE 9. Pressure contours (----, $Re_H = 115000$; ......, $Re_H = 30000$).

section III, the wall shear stress remains weak. An increase in cross-sectional area results in decreasing velocities, this effect being particularly noticeable in the core region ($y^+ > 100$). So, velocity distributions are distorted but remain generally below the universal curve. These results are similar to those obtained by Nikuradse and by Okwuobi & Azad (1973) and Khabakhpasheva, Yefimenko & Gruzdeva (1978) in a conical diffuser. At section IV, the wall shear stress reaches a value close to that corresponding to the equivalent straight tube; as a result, velocity distributions are grouped around the universal log law. One can also notice that, compared with the other sections, discrepancies between calculated and measured profiles are less noticeable. Of course, the constant flow rate implies the periodic increase and decrease of velocity profiles as previously described. This is a geometrical consequence independent of any closure hypothesis on the Reynolds stress.

Generally, numerical predictions give the same trends as experimental measurements with regard to the relative position of mean-velocity profiles compared to the straight tube profiles and with regard to their evolution between two successive crests. Nevertheless, there are discrepancies for the actual magnitudes of the mean velocities.

The non-existence of a dynamic-equilibrium region seems to be a direct consequence of the complex character of the flow as it undergoes variable curvature effects and

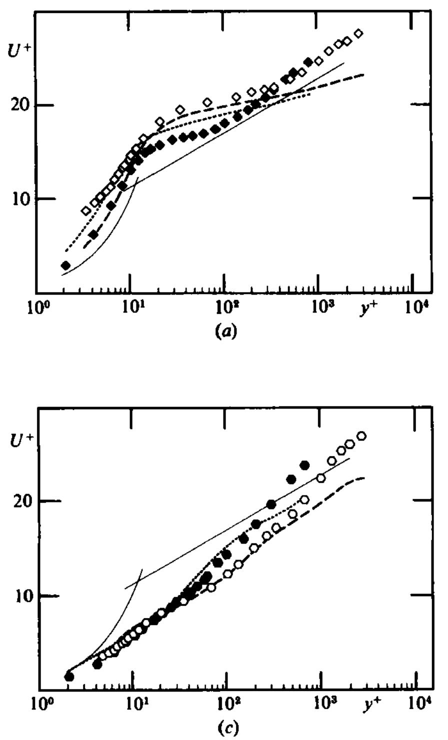

FIGURE 10. Mean-velocity profiles: (*a*) Section I; (*b*) section II; (*c*) section III; (*d*) section IV. $Re_H = 30000$ (◆, ●, ⬢, ▼ experiments, ... calculation); $Re_H = 115000$ (◇, ○, ⬡, ▽, experiments, ---- calculation). —— straight-pipe universal profile.

is in continuous reorganization. It should be noted that the above discrepancies are less marked at a Reynolds number of 115000.

It is worth noting the calculation in Jackson & Hunt (1975) and Sykes (1980) for the turbulent-boundary-layer flow over a small hump with shallow slope. These authors find that an inner layer exists close to the surface where the stresses are always in equilibrium. Outside this region the Reynolds stresses are subjected to a strong distortion. The inner region turns out to have a thickness of order $U_* L/U_0$ which, for the values in a pipe ($L \simeq a$, $U_0 \simeq \bar{U}_H$), reduces to a layer of depth less than 2 mm, which corresponds precisely to the depth of the viscous and transition regions. Consequently this fact confirms the non-existence of an equilibrium zone.

4.1.3. *Wall region*

Figures 11 (*a*)–(*f*) show the mean-velocity profiles for $y^+ < 50$ on a linear plot, with U_{*H} as the reference velocity. We have drawn for comparison the representative curve of the empirical relation given by Spalding (1961).

$$y^+ = u^+ + B\left[\exp \chi u^+ - 1.0 - \chi u^+ - \frac{(\chi u^+)^2}{2!} - \frac{(\chi u^+)^3}{3!} - \frac{(\chi u^+)^4}{4!}\right]$$

(with $B = 0.1108$ and $\chi = 0.04$) and recommended by Hinze for flows on a flat plate. Measured and calculated profiles are distributed on both sides of the Spalding relation according to variations in wall curvature. In the diverging part of the duct ($4\lambda < x \leqslant 4\lambda + \frac{1}{2}\lambda$) experimental measurements very near the wall are only indicative,

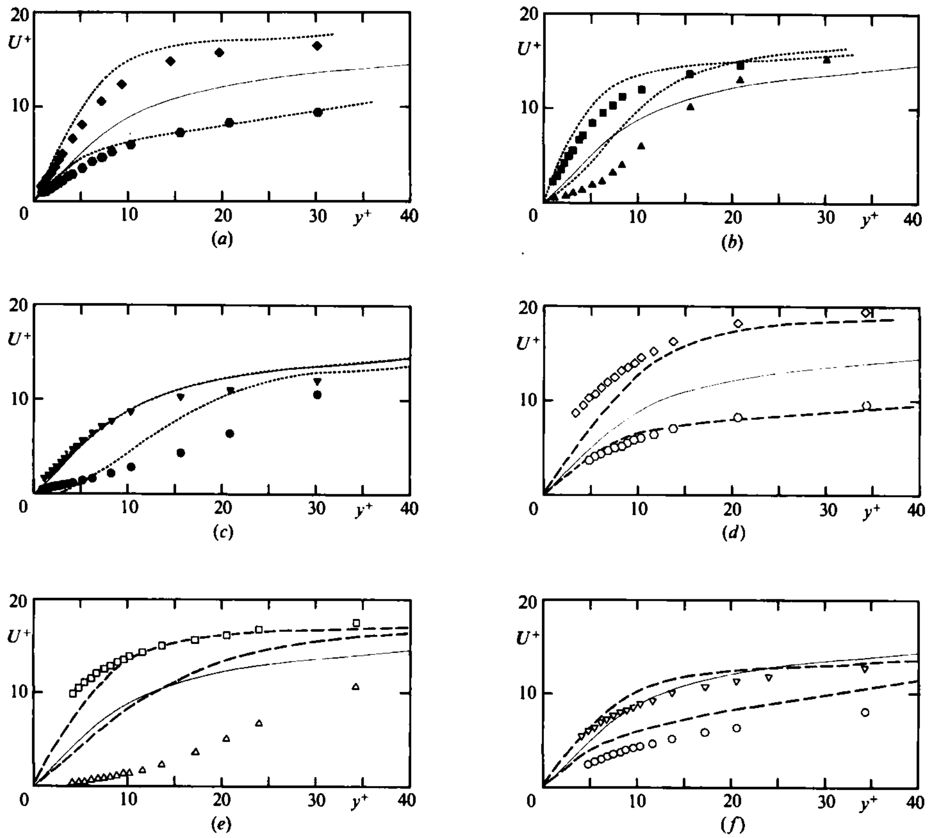

FIGURE 11. Near-wall mean-velocity profiles. (*a*), (*b*), (*c*): $Re_{\mathrm{H}} = 30000$ (experiments: sections 4λ(I), ◆; $4\lambda+\frac{1}{2}\lambda$(III), ⬢; $4\lambda+\frac{1}{8}\lambda$, ▲; $4\lambda+\frac{7}{8}\lambda$, ■; $4\lambda+\frac{1}{4}\lambda$(II), ●; $4\lambda+\frac{3}{4}\lambda$(IV), ▼; calculation, ...). (*d*), (*e*), (*f*). $Re_{\mathrm{H}} = 115000$ (experiments: sections 4λ(I), ◇; $4\lambda+\frac{1}{2}\lambda$(III), ⬡; $4\lambda+\frac{1}{8}\lambda$, △; $4\lambda+\frac{7}{8}\lambda$, □; $4\lambda+\frac{1}{4}\lambda$(II), ○; $4\lambda+\frac{3}{4}\lambda$(IV), ▽; calculation, ---). —— straight-pipe profile.

because of the occurrence in this region of non-stationary reverse flows that disturb the measurements: in fact, the hot-wire sensor is only sensitive to the modulus of the velocity vector. All experimental results presented here are corrected for the effect of wall proximity (Chauve 1980). For $Re_{\mathrm{H}} = 30000$ and $y^+ < 20$, measured profiles and calculated profiles (figures 11*a–c*) are in the same relative positions. On figures 11(*b*, *c*), we notice that velocity profiles exhibit an inflection point, with a region of negative velocities for the calculated distribution at section $4\lambda+\frac{1}{4}\lambda$. For $Re_{\mathrm{H}} = 115000$ and $y^+ < 20$, except for section $4\lambda+\frac{1}{8}\lambda$, the relative positions of profiles (figures 11*d–f*) are identical. The calculated profile at section $4\lambda+\frac{1}{8}\lambda$ is slightly distorted compared with the measured distribution: also the calculation does not indicate negative velocities. The smallest velocity occurs at section $4\lambda+\frac{1}{8}\lambda$, which corresponds in practice to the location of the inflection point of the wall undulation. Negative velocities are found at $Re_{\mathrm{H}} = 30000$. This result is clearly shown in figures 12(*a*, *b*) which feature a velocity-vector plot in the near-wall region. It appears that, in the converging part of the flow and very close to the wall, velocity vectors are parallel to the wall and correspond with its curvature, even though in the diverging part some deviations appear which reveal the appearance of recirculating flows at a Reynolds number of 30000 (figure 12*a*).

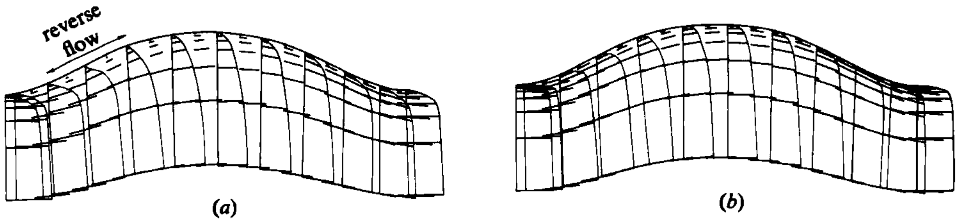

FIGURE 12. Velocity vector plots: (a) $Re_H = 30000$; (b) $Re_H = 115000$.

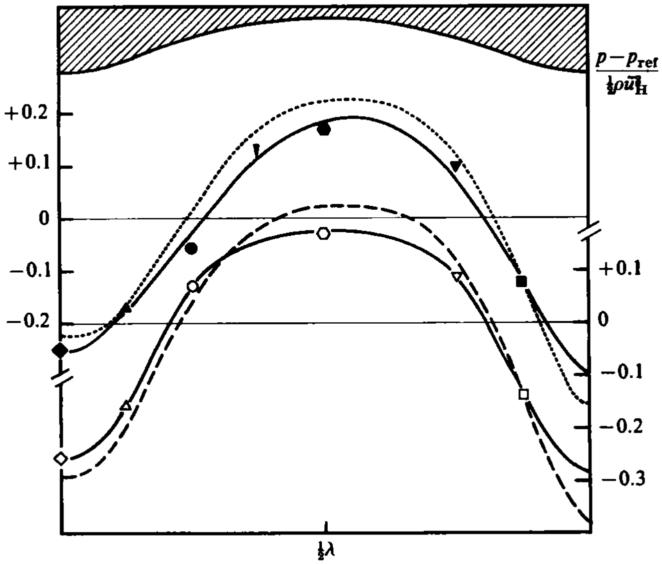

FIGURE 13. Pressure evolution along pipe wall. $Re_H = 30000$ (◆——■, experiments; ......, calculation); $Re_H = 115000$ (◇——□, experiments; ----, calculation).

Near the wall, the comparison between pressure values extrapolated from measured radial distributions and calculated values (figure 13) shows good agreement at the two Reynolds numbers under consideration. For $Re_H = 30000$, these distributions of limiting values at the wall are more dissymmetrical than for $Re_H = 115000$; this may be caused by the distortion of the velocity field due to the reverse-flow region (Hsu & Kennedy 1971). Along the axis of the model, the amplitude of pressure variations is reduced by a factor of about 10. It appears then, that weak amplitude wall undulations produce an effect on the near-wall pressure field which is one order of magnitude larger than the pressure drop between two successive crests. Indeed, this depends very much on the flow velocity and horizontal lengthscale.

From mean-velocity measurements within the viscous sublayer we obtained friction coefficients, plotted in figure 14 along with calculated values, which are in qualitative agreement. In particular, the extrema are practically at the same location, although they attain higher values in the calculation. The minimum occurs in the diverging part of the duct and the maximum in the converging part just after the inflection points of the wall waviness (Hsu & Kennedy 1971; Thorsness *et al.* 1978; Zilker, Cook & Hanratty 1977). The smallest values of $\lambda_*(x)$ correspond to the region of the flow where instantaneous reverse flow occurs. The extent of this region appears

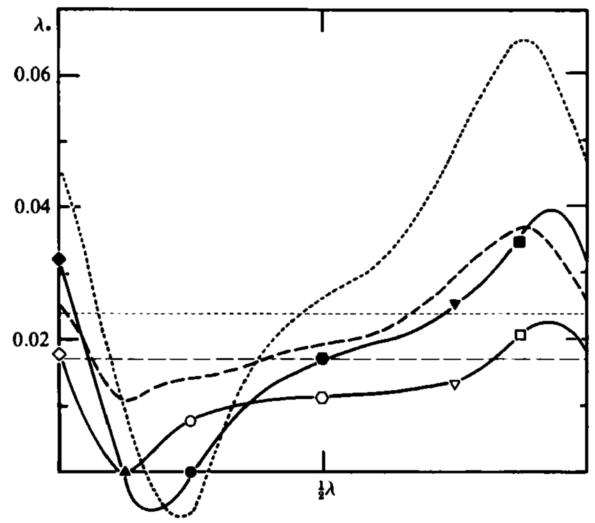

FIGURE 14. Wall-shear-stress coefficient $\lambda_* = 8\tau_P/\rho\bar{u}^2$. $Re_H = 30000$ (◆——■, experiments; ......, calculation; ----, Blasius coefficient for straight pipe). $Re_H = 115000$ (◇——□, experiments; ——, calculation; ———, Blasius coefficient for straight pipe).

to be controlled by Reynolds number (Eaton, Johnston & Jeans 1979). Indeed, pressure and velocity measurements, along with friction coefficient distributions, corroborate the essential role of this parameter; an increase in Reynolds number results in a collapse of the reverse-flow region. This effect seems consistent with an increase in turbulent transfer at high Reynolds numbers. The notion that one can move from a separated to a non-separated region by increasing flow rate is suggested by the analysis of Zilker & Hanratty (1979) who plot the evolution of amplitude–length ratio $(2\pi\nu/\lambda U_*)$ *versus* dimensionless wavenumber in various situations. The values of dimensionless wavenumber for present cases are 5.4×10^{-3} for $Re_H = 30000$ and 1.7×10^{-3} for $Re_H = 115000$, falling respectively in the separated and the non-separated zone delimited in Zilker & Hanratty's (1979) diagram. Although experimental and calculated results (figure 14) are qualitatively similar, the quantitative differences between the two Reynolds-number cases are not predicted.

The existence of a region near the wall where unsteady reverse flow occurs downstream of every crest has been confirmed by signal analysis from the special hot-wire–cold-wire probe (§2.3). This analysis shows clearly the spreading of this region downstream of the inflection point of the wall undulation and the growth with decreasing Reynolds number (Chauve & Schiestel 1981; Eaton *et al.* 1979). Visualizations made in water confirm all the results obtained in air (Chauve 1981; Chauve & Schiestel 1981). Also, dye injection at the wall at several sections along an undulation has shown the non-stationary character of observed reverse flow. The existence of reverse flow has been clearly established between the $4\lambda + \frac{1}{8}\lambda$ and $4\lambda + \frac{1}{2}\lambda$ sections (figure 15, plate 1), the injected dye never flowing upstream beyond the $4\lambda + \frac{1}{8}\lambda$ section, which corresponds to the wall inflection point. However, these visualizations did not allow a precise definition of the location downstream where no reverse flow occurs. The characteristics of the hydrodynamic gravity-fed tunnel at the IMST precluded experiments at $Re_H = 115000$.

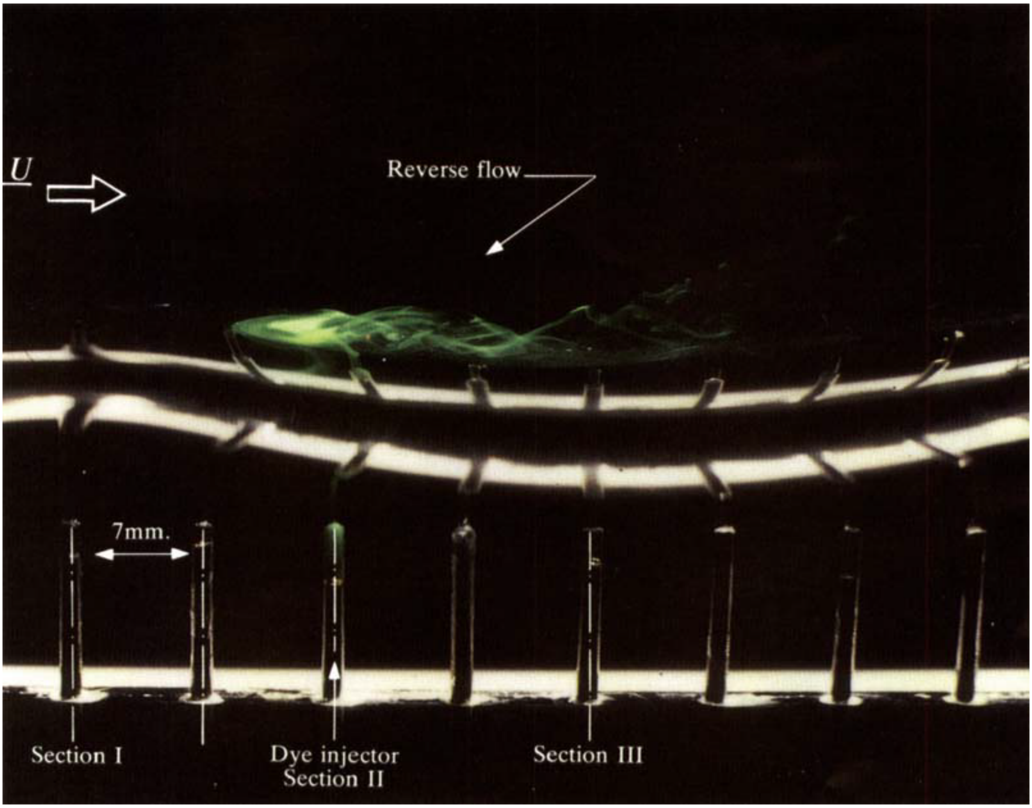

FIGURE 15. Instantaneous picture of reverse flow.

4.1.4. *Momentum balance*

In order to determine the contribution of friction forces to the overall head loss over an undulation, we considered each term in the momentum balance equation.

The following general equation, written for a volume $\mathscr{V}$ of fluid bounded by a surface $\mathscr{S}$:

$$\iiint_{\mathscr{V}} \partial_t(\rho U_i)\,\mathrm{d}\mathscr{V} + \iint_{\mathscr{S}} \rho U_i\, U_j n_j\,\mathrm{d}\mathscr{S} = \iint_{\mathscr{S}} \sigma_{ij} n_j\,\mathrm{d}\mathscr{S} + \iiint_{\mathscr{V}} f_i\,\mathrm{d}\mathscr{V} \tag{1}$$

is applied to the case of a domain bounded by the lateral undulated wall and by two cross-sections Σ_u and Σ_d located at two consecutive crests. The lateral undulated wall will be denoted by Σ_l. Equation (1) is now written, after projection to the longitudinal axis, taking into account stationarity and periodicity hypotheses and neglecting body forces:

$$\iint_{\Sigma_\mathrm{l}} \tau_{1j} n_j\,\mathrm{d}\mathscr{S} - \iint_{\Sigma_\mathrm{l}} p n_1\,\mathrm{d}\mathscr{S} + \iint_{\Sigma_\mathrm{u}} p\,\mathrm{d}\mathscr{S} - \iint_{\Sigma_\mathrm{d}} p\,\mathrm{d}\mathscr{S} = 0, \tag{2}$$

with $\sigma_{ij} = -p\delta_{ij} + \tau_{ij}$ and $\tau_{ij} = \mu(U_{i,j} + U_{j,i})$ where $U_{i,j}$ stands for covariant derivative given in § 3.3. Equation (2) can also be written:

$$-F + G + \pi a^2(0)\,(\mathscr{P}_\mathrm{u} - \mathscr{P}_\mathrm{d}) = 0. \tag{3}$$

Since the wall curvature remains very weak, it can be assumed to a good approximation that $F \simeq -\mu \iint_{\Sigma_\mathrm{l}} U_{1,2}\, n_2\,\mathrm{d}\mathscr{S}$.

After normalization we obtain:

$$\frac{\tilde{\tau}_p}{\rho \tilde{u}_\mathrm{H}^2} - \frac{\iint_{\Sigma_\mathrm{l}} p \sin\alpha\,\mathrm{d}x}{\rho \tilde{u}_\mathrm{H}^2\,\lambda} + \frac{a(0)}{2\lambda}\,\frac{\mathscr{P}_\mathrm{u} - \mathscr{P}_\mathrm{d}}{\rho \tilde{u}_\mathrm{H}^2}; \tag{4}$$

$$\tfrac{1}{8}\varLambda_{*\mathrm{F}} - \tfrac{1}{8}\varLambda_{*\mathrm{P}} + \tfrac{1}{8}\varLambda_{*} = 0. \tag{5}$$

The terms in (5) have been calculated both from numerical results and from experimental results and are given in table 2.

Equation (5) applied to the case of the equivalent straight tube gives:

$$\tfrac{1}{8}\varLambda_{*\mathrm{F}} = \tfrac{1}{8}\varLambda_{*\mathrm{H}}. \tag{6}$$

If we use the Blasius formula we obtain $\frac{1}{8}\varLambda_{*\mathrm{H}} = 0.003$ at $Re_\mathrm{H} = 30000$, and $\frac{1}{8}\varLambda_{*\mathrm{H}} = 0.00215$ at $Re_\mathrm{H} = 115000$. Owing to experimental difficulties in determining $\varLambda_{*\mathrm{F}}$ and uncertainties in estimating the limiting wall values of pressure in the $\varLambda_{*\mathrm{P}}$ determination, it was not possible to get an exact experimental balance.

In the case of a tube with an undulated wall, the overall head loss between two consecutive crests is compensated on the one hand by viscous friction forces and on the other hand by pressure forces on the lateral wall boundary. It is found that this overall head loss is about twice that which would exist in an equivalent straight tube in which only viscous friction forces act. More precisely, wall undulations produce pressure forces on lateral boundaries that are larger in magnitude than the increase in wall friction (compared to the straight tube case).

4.1.5. *Remarks on wall-curvature effects*

The most important effects of wall curvature are not those that appear explicitly in the momentum equations but the indirect effects that influence the turbulence field. These latter are often an order of magnitude larger than the mere inclusion of explicit

	Calculations		Experiments	
Reynolds number	30000	115000	30000	115000
$(\frac{1}{8}\Lambda_* \times 10^2$	0.583	0.401	0.772	0.336
$(\frac{1}{8}\Lambda_{*\mathrm{F}}) \times 10^2$	0.390	0.278	0.166	0.158
$(\frac{1}{8}\Lambda_{*\mathrm{P}}) \times 10^2$	0.193	0.123	0.255	0.0424

TABLE 2.

additional terms would lead one to believe (Bradshaw 1973). Experiments in a boundary layer over a curved wall show that the turbulence level is increased on a convex wall and is decreased on a concave wall. It was thus of interest to the present case to try to estimate curvature effects on the dynamic field.

We introduce the Richardson number:

$$Ri = 2S(1+S),$$

where

$$S = \frac{U/r}{\partial U/\partial r}.$$

The sign of this number governs the stability of the flow (Bradshaw 1969). One can then consider a fluid particle A. This particle is shifted from its equilibrium position and we observe the different forces that act upon it (Di Prima & Swinney 1981; Tritton & Davies 1981):

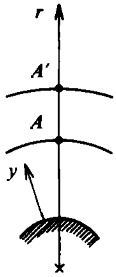

with $\overset{*}{U} \equiv$ 'particle' velocity

$U \equiv$ fluid velocity

they are

the centrifugal force: $\rho \dfrac{\overset{*}{U}{}^2_{\mathrm{A}'}}{r_{\mathrm{A}}+y} = \rho \dfrac{r^2_{\mathrm{A}}\, U_{\mathrm{A}}}{(r_{\mathrm{A}}+y)^3}$,

the pressure force: $\left(\dfrac{\partial p}{\partial r}\right)_{\mathrm{A}'} = \rho \dfrac{U^2_{\mathrm{A}'}}{r_{\mathrm{A}}+y}$,

the inertial force: $\rho \ddot{y}$.

After linearization we obtain:

$$\ddot{y} + \frac{2U_{\mathrm{A}}}{r^2_{\mathrm{A}}} \left| \frac{\partial ur}{\partial r} \right|_{\mathrm{A}} y = 0.$$

If $\partial ur/\partial r > 0$ the solution is periodic and bounded and viscosity damping ensures stability. If $\partial ur/\partial r < 0$ the solution is unbounded, the particle moves away from its equilibrium position: this case is unstable.

In order to take into account curvature effects within the framework of the k-ϵ

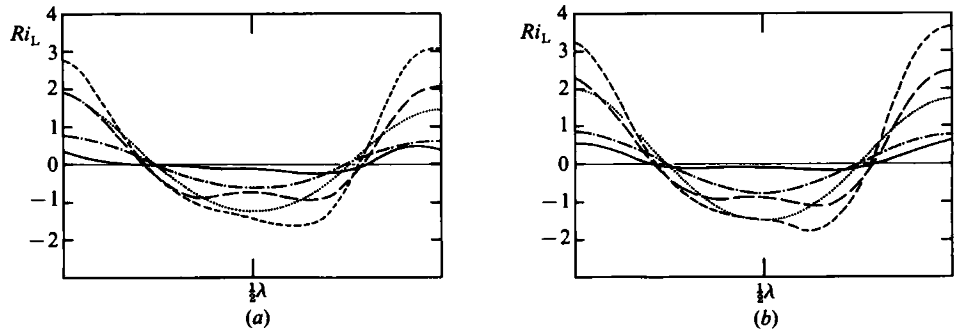

FIGURE 16. Richardson number distribution. (*a*) $Re_H = 30000$, (*b*) $Re_H = 115000$ ($r/a(x) = 0.28$, —·—·—; 0.50, ...; 0.90, ----; 0.96, – – –; 0.996, ——).

model, Launder proposed to modify the numerical constant $c_{2\epsilon}$ by multiplying it by $(1-0.25\,Ri_L)$ where Ri_L represents a modified Richardson number defined by

$$Ri_L = 2\frac{k^2}{\epsilon^2}\frac{U_1}{r}\frac{\partial U_1 r}{\partial r}.$$

In this expression the timescale $(\partial U/\partial r)^{-1}$ has been replaced by k/ϵ, thus the modified Richardson number remains finite even when $\partial U/\partial r$ goes to zero.

For the present undulated model we chose the latter definition with the curvature parameter $S = (U_1/\mathscr{R})/(\partial U_1/\partial \xi_2)$ where $\mathscr{R}$ represents the local radius of curvature of the longitudinal coordinate and ξ_2 is the curvilinear abscissa in orthogonal coordinates. We obtain finally:

$$Ri_L = \frac{2k^2 U_1/\mathscr{R}}{\epsilon^2}\left[\frac{\partial U_1}{\partial \xi_2}+\frac{U_1}{\mathscr{R}}\right].$$

In figures 16(*a*, *b*) we plot, for two Reynolds numbers (30000 and 115000), the distribution of Ri_L between two consecutive crests and for five values of the ratio $r/a(x)$. In the bulk of the flow associated with the smallest values of $\partial U_1/\partial \xi_2$, the longitudinal distribution of Ri_L ($r/a(x) = 0.28$) essentially reflects the influence of streamline curvature. The maximum amplitude occurs at $r/a(x) \simeq 0.9$, a region with high curvature and still with high velocities. Very near the wall ($r/a(x) \simeq 0.996$) Ri_L changes sign at a location which becomes increasingly close to that of the wall inflection point. Roughly, there is no significant difference between Ri_L distributions for the two Reynolds numbers under consideration. However, for $r/a(x) = 0.996$ at $Re_H = 30000$ the reverse-flow region causes a distortion of streamlines and thus the curvature effect is masked; the curvature effect appears more distinctly at the same ordinate in the converging part of the duct. At $Re_H = 115000$, collapse of the reverse-flow region yields an almost symmetrical distribution of Ri_L at $r/a(x) \simeq 0.996$, which follows closely the wall curvature.

Lastly, we point out that the modification to $C_{2\epsilon}$ in the transport equation of the dissipation rate of turbulent energy produced only moderate changes in the numerical results. Although the values of this modified coefficient vary from about 1 to 3 around the usual value 1.9, the periodicity of the wall undulations characterized by successive changes in wall curvature produces successive changes in the sign of Ri_L that smooth and strongly reduce local curvature effects if they are compared with those in turbulent shear flows with constant wall curvature (Alcaraz, 1977). Taylor *et al.*

(1976) arrived at the same conclusion concerning the flow above fixed rough wavy surfaces for which the surface-shear-stress distribution is not dramatically changed by Richardson modification but, rather, strongly influenced by undulation shape. The characteristic response time of the turbulent field k/ϵ is greater than the characteristic time of the flow λ/U. Thus, the evolution of the turbulent field cannot respond directly to the periodic action of the undulated wall.

4.2. *Turbulent field*

4.2.1. *Turbulent kinetic energy*

We found that the mean measured and calculated turbulent energy levels are higher than in a straight tube at the same Reynolds number (Laufer 1954). This increase in turbulent energy reaches about 30% for $R_{\mathrm{H}} = 30000$ and about 15% for $Re_{\mathrm{H}} = 115000$ at $r/a(x) \simeq 0.1$ (Chauve & Schiestel 1981). The experimental determination of the three normal stresses (Chauve 1981), has shown in particular that large values of kinetic energy were mainly due to a rise in longitudinal velocity correlation $\overline{U'^2}$ caused by the presence of undulations. Moreover, experiments did not show significant influence of undulation on $\overline{V'^2}$ and $\overline{W'^2}$ components away from the wall. This result is at variance with Britter, Hunt & Richards, (1981), who predicted that in the boundary layer over a two-dimensional roughened hill $\overline{U'^2}$ decreased and $\overline{V'^2}$ increased over the crest. The variations in turbulent kinetic energy between two successive crests are given in figure 17(*a*, *b*). In the region of the flow accessible to measurements, we found satisfactory agreement between experimental results and numerical predictions. For $y^+ \geqslant 100$, we did not find the distinctly different behaviour in the decelerated and accelerated parts which has been encountered by Rodi & Scheuerer (1983). These authors found it useful to modify the equation to correct partially this spurious behaviour. In the wall region, which is not easily accessible to X-probes, calculations have shown that a sharp peak of energy begins to grow in the region where reverse flow occurs. This local energy growth is then progressively absorbed by the neighbouring downstream region. The peak of energy is located between sections $4\lambda + \frac{1}{4}\lambda$ and $4\lambda + \frac{3}{8}\lambda$ in the diverging part of the duct.

These results are quite well illustrated by figure 18(*a*, *b*), which represent contour plots of kinetic energy in the near-wall region. We notice that the effect of increasing the Reynolds number is a squeezing of the contour lines against the wall. Longitudinal distributions of the turbulent energy normalized by its value at the crest, are shown in figure 19 for a radius equal to 0.98 $a(x)$, a value that corresponds roughly to the location of the maximum kinetic energy at each section. These distributions between two crests are very different from those suggested by mere converging and diverging effects. In fact, in a diverging duct, the turbulent-energy level decreases steadily (Okwuobi & Azad 1973); the behaviour is reversed in a converging duct.

In the present case, the evolution conjectured previously is disturbed from the inflection point of the wall undulation down to the next crest because of reverse flow. The magnitude of the variations is more important at a Reynolds number of 30000, for which reverse flow is intensified. If we look at the numerical results obtained with the modified k-ϵ model, taking into account curvature effects through a Richardson number, very few changes were produced on the energy-field values compared with initial calculation. The only significant changes occur near the wall but remain relatively modest (figure 19). Referring to §4.1.5, we know that a turbulent flow on a concave wall ($Ri < 0$) is unstable and turbulent energy is increased, while a turbulent flow on a convex wall ($Ri > 0$) is stable and turbulent energy is decreased

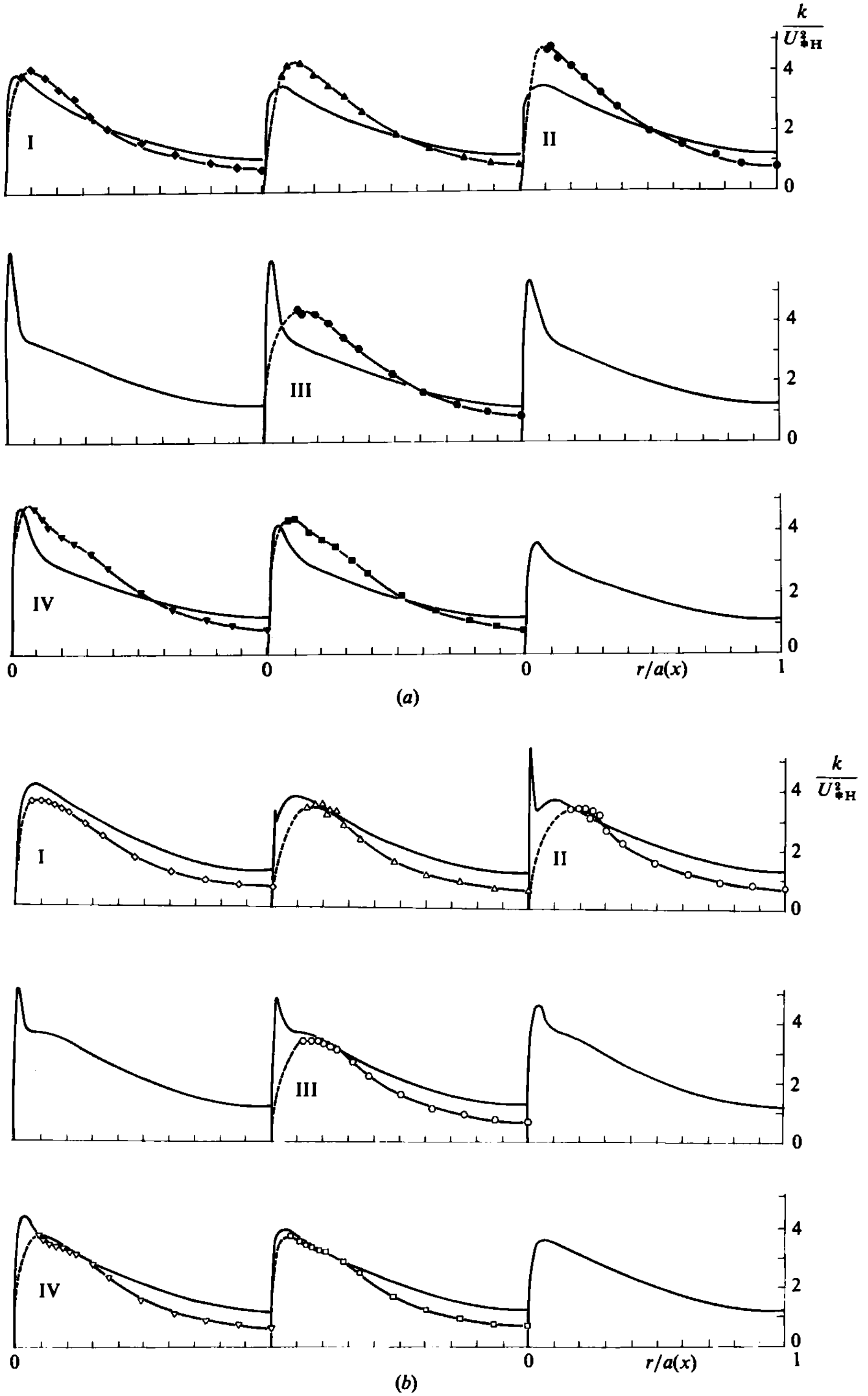

FIGURE 17. Turbulent kinetic energy profiles: (*a*) $Re_H = 30000$ (◆ to ■, experiments; ——, calculation); (*b*) $Re_H = 115000$ (◇ to □, experiments; ——, calculation) for sections $4\lambda + j\lambda/8$ ($j = 0$ to 8).

FIGURE 18. Contour plots of turbulent kinetic energy: (*a*) $Re_H = 30000$; (*b*) $Re_H = 115000$.

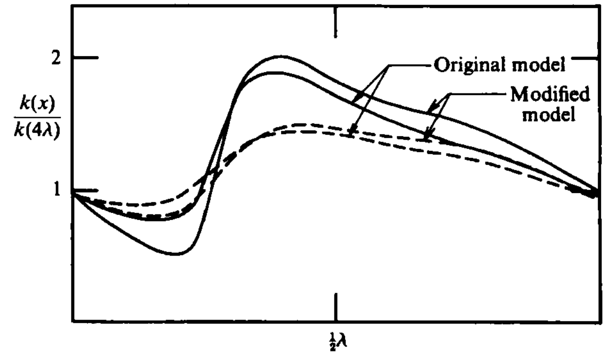

FIGURE 19. Effect of Richardson number on $k(x)/k(4\lambda)$ for $r/a(x) = 0.98$ (——, $Re_H = 30000$; ---, $Re_H = 115000$).

(Di Prima & Swinney 1981; Tritton & Davies 1981). This result is quite perceptible in figure 19, but some time lag is introduced between the turbulent-field evolution and the periodic cross-section variations that act upon it, a turbulence-memory effect.

4.2.2. *Turbulent shear stress*

Distributions of turbulent shear stress between two successive crests are plotted in figure 20(*a*,*b*) for both Reynolds numbers. The general shape of the curves is similar to the kinetic-energy distributions but there is a marked difference between experimental and numerical values obtained near the crest. Negative values have been obtained at some locations and these discrepancies seem to be a consequence of the turbulent-viscosity hypothesis which relate turbulent stresses to the mean velocities at a point. In fact, local excess velocities developing near the crest modify the values of $\partial U/\partial y$ and can lead to $\partial V/\partial x$ values that are not negligible, so that R_{12} may become negative. This consequence seems to be inconsistent with experimental results and appears to be an intrinsic limitation of the k-ϵ model based on the turbulent-viscosity concept. Except for cross-sections near the crest, the agreement between computation and experiment is satisfactory. Moreover, calculations have shown the development near the wall of a sharp peak which grows in the reverse-flow region, as observed in kinetic-energy profiles. Relative values of shear stress are lower at a Reynolds number of 115000 than at 30000. Also, radial distributions of R_{12}/U^2_{*H} that, in the fully turbulent part of the flow, can be identified with the total shear, are Reynolds-number dependent, contrary to what is found in a straight tube (Laufer

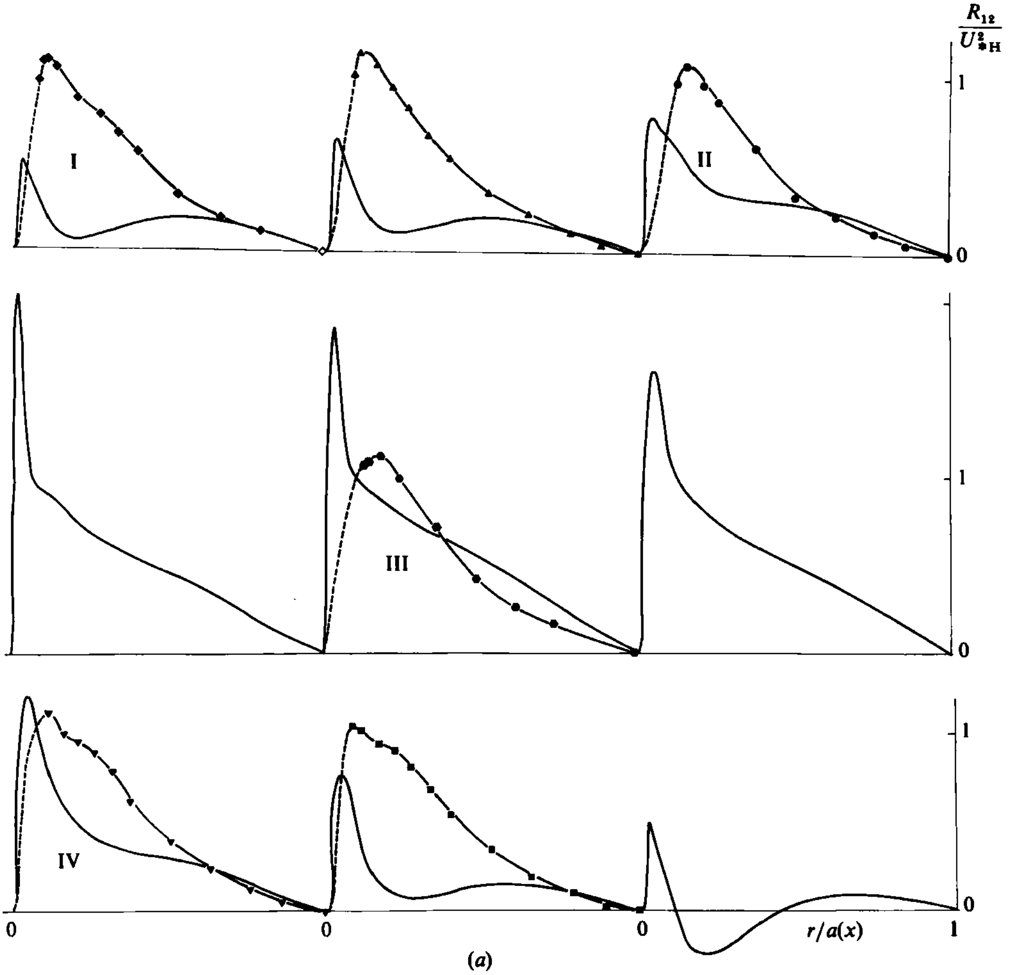

FIGURE 20(*a*). For caption see next page.

1954). The S-shaped curve crossing the linear distribution for the straight tube is characteristic of the effect of undulations (Hsu & Kennedy 1971).

The absence of an inertial-equilibrium region in the undulated tube led us to consider the magnitude of the shear stress/turbulent intensity ratio $-\overline{U'V'}/2k$ in the present flow. For an equilibrium layer this ratio is equal to about 0.15 (Hinze 1975). For several values of $r/a(x)$ we calculated the mean value of this ratio over a wavelength. This result, plotted in figure 21, effectively indicates the global effect of the undulations. Straight-tube results (Laufer 1954) are also plotted for comparison. Experimental values of this ratio are always smaller than the value obtained in a straight tube. The same result is predicted numerically. Agreement between prediction and experiment is especially good in the bulk of the flow. In the wall region, discrepancies between calculations and experiments may be due to differences in shear-stress distributions already noticed near the crest of the undulations. The Reynolds-number effect is particularly appreciable at a radius larger than 0.5 $a(x)$ and results in an increase of this ratio with increasing Reynolds numbers, which is opposite to what is observed in a straight tube.

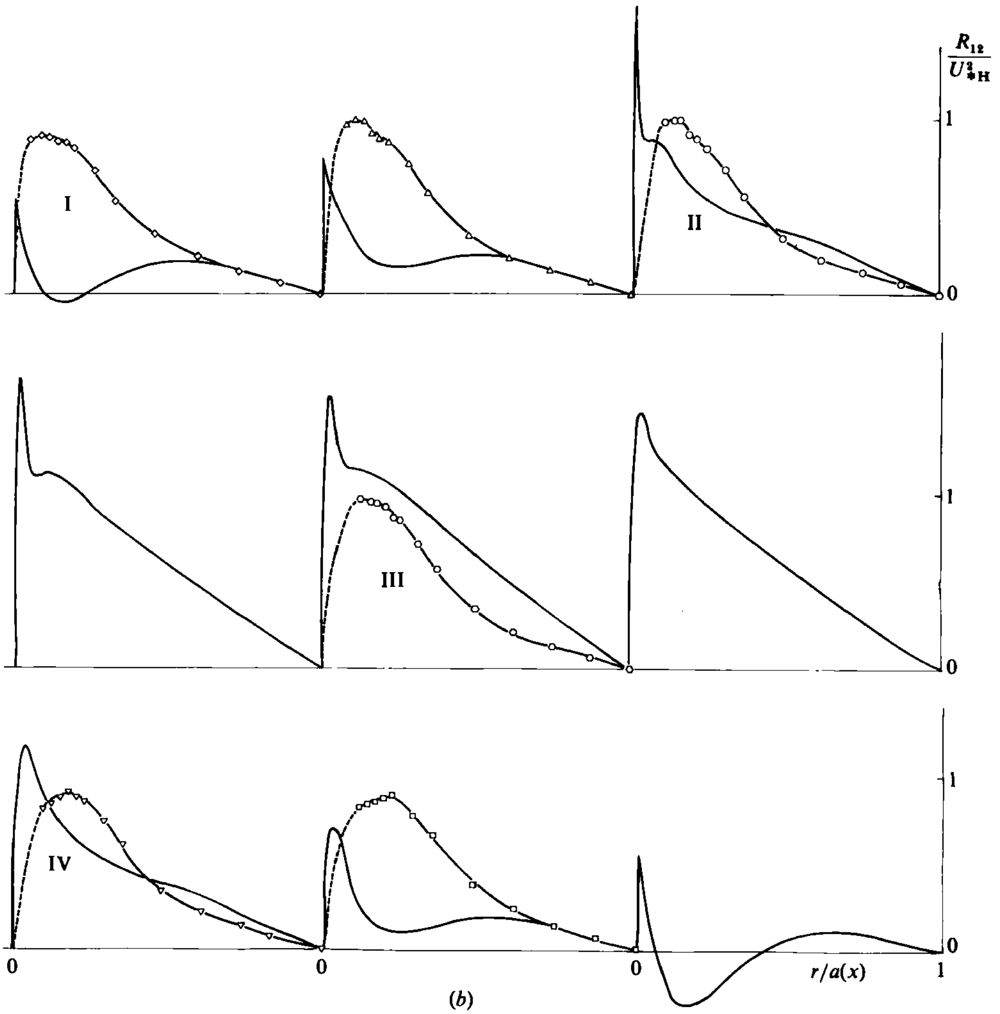

FIGURE 20. Turbulent shear stress distribution. (*a*) Re_H = 30000 (◆ to ■, experiments; ——, calculation). (*b*) Re_H = 115000 (◇ to □, experiments; ——, calculation).

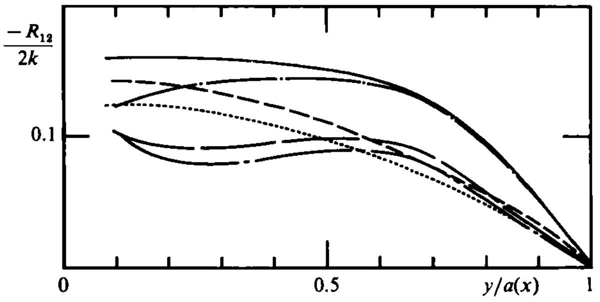

FIGURE 21. Longitudinal mean value of anisotropy coefficient: Re_H = 30000 (......, experiments; —·—·—, calculation); Re_H = 115000 (– – – –, experiments; ———, calculation); Laufer measurements (——, Re_H = 40500; —·—·—, Re_H = 427500).

5. Concluding remarks

An experimental study, including measurements in air and visualizations in water, and a numerical prediction based on a k-ϵ model have been developed for a complex turbulent shear flow: the turbulent flow through an axisymmetrical duct having streamwise periodic wall undulations with small amplitude and a wavelength of the order of magnitude of its mean diameter. The methodology has been described and a description given of the mean-velocity and pressure fields as well as of the turbulent-velocity field. In particular, mean velocities have been measured within the viscous sublayer and corrected for the effect of wall proximity on the hot wire. The wall friction has been deduced from these measurements.

One of the main characteristics of this flow is the existence of flow reversal revealed by the use of a special two-wire probe and by flow visualization. The leading parameter is the flow Reynolds number which determines the extent and the intensity of flow reversal and in turn the mean distributions of pressure and velocity.

Turbulent transfer, increasing with Reynolds number, is likely to reduce very strong reverse flows and at the same time to move the reattachment point upstream. Numerical predictions also account for this phenomenon. Moreover, calculations carried out in laminar flow have shown the opposite effect.

Head losses at Reynolds numbers of 30000 and 115000 are respectively multiplied by a factor of about 2.5 and 1.5 if they are compared to head losses in a straight tube with the same respective flow rates.

Radial distributions of pressure, between two successive crests, reflect wall-curvature variations. Moreover, pressure variations near the wall are found to be an order of magnitude higher than the mean-pressure drop over an undulation. As for mean-velocity distributions their evolution is governed by divergent–convergent effects in the duct. This dependence does not allow the establishment of an inertial-equilibrium region within the flow which is undergoing continuous organization.

The previous observations are supported by wall-shear-stress distributions: regions where the shear stress is either zero or very small are reduced when the velocity is increased. However, over an undulation, the mean wall shear stress remains below the value in an equivalent cylindrical duct. This wall-shear-stress evolution along an undulation is well described qualitatively by calculations and in particular the experimental locations of extrema are predicted correctly.

Experimental results for the turbulent field have been obtained from single- and cross-wire measurements of velocity fluctuations. From these measurements, radial distributions of the turbulent kinetic energy were obtained at several cross-sections between two successive crests. It appears that the mean-energy level is distinctly higher than that which prevails in a straight tube at the same Reynolds number. This result is reinforced by numerical calculations. Experiments have shown (Chauve 1981) that this increase in turbulence energy is associated with large values of the longitudinal velocity fluctuation. Numerical predictions allowed more accurate insight into local curvature effects. In the vicinity of the wall, a region that is not accessible to measurement, these effects result in the growth of an energy peak within the diverging part of the duct and near the inflection point of the wall. The use of a curvature Richardson number in the turbulence model resulted in only a few changes in the numerical results. Turbulent-shear-stress distributions do not exhibit the linear behaviour found in a straight tube. The observed distributions are S-shaped and are lower near the axis and higher near the wall compared with the straight-tube results. This kind of distribution is typical of undulation effects. Calculations have strongly overpredicted this effect in the immediate neighbourhood of the crest.

The comparison between experiments and calculations indicates that the model we used has some shortcomings for a detailed description of the turbulent field; it does however permit a good estimate of global mean values. Further, numerical predictions are, roughly speaking, more satisfactory at a Reynolds number of 115000 for which the reverse flow is weaker. Taking into account curvature effects through a Richardson number as proposed by Launder (1975) did not noticeably improve the numerical predictions. We recall in particular that numerical calculations have allowed the prediction of a recirculating-flow zone which extends beyond the point of inflection at the wall as well as the effect of Reynolds number on this zone. Since numerical predictions efficiently yield a fair description of the most important mean values, the k-ϵ model thus allows extrapolation of experimental results to similar cases by varying geometrical and dynamical parameters of the problem, for which experimental investigations would be long and expensive.

It thus appears that at the present time, in such a complex flow, the k-ϵ model remains a good compromise between reliability of predictions and universality of applicability. In fact, it can give overall agreement between experiments and calculations, but the detailed behaviour of some local quantities can be wrong, as it is the case here for vertical stress distributions at the crests.

Improvement of numerical predictions would require a more complete description of the turbulent field, but such an approach would necessitate the development and testing of new and more elaborate prediction methods.

The work reported herein has been supported by 'Commissariat à l'Energie Atomique' (C. E. N. Saclay, France). This support is gratefully acknowledged.

REFERENCES

ALCARAZ, E. 1977 Contribution à l'étude d'un jet plan turbulent évoluant le long d'une paroi convexe à faible courbure. Thèse Doct. Es. Sc. Phys. University Claude Bernard, Lyon, France.

AMSDEN, A. A. & HARLOW, F. H. 1970 *Los Alamos Scient. Lab. Rep. LA* 4370, University of California.

ANTONIA, R. A., CHAMBERS, A. J. & HUSSAIN, A. K. M. F. 1980 *Phys. Fluids* **23**, 821–824.

BRADSHAW, P. 1969 *J. Fluid Mech*, **36**, 177–191.

BRADSHAW, P. 1973 *Agardograph* 169.

BRITTER, R. E., HUNT, J. C. R. & RICHARDS, K. J. 1981 *Q. J. R. Met. Soc.* **107**, 91–110.

BRUN, E. A., MARTINOT-LAGARDE, A. & MATHIEU, J. 1968 *Mécanique des Fluides.* Paris: Dunod.

CHAUVE, M. P. 1980 *Euromech Colloquium 132, Lyon, France, July 2–4.*

CHAUVE, M. P. 1981 Etude expérimentale d'un écoulement turbulent en conduite axisymétrique à paroi poreuse ondulée. Thèse Doct. Es. Sc. Phys. University Aix Marseille II, France.

CHAUVE, M. P. & SCHIESTEL, R. 1981 *Third Symp. on Turbulent Shear Flows, Univ. of Calif. Davis, Sept.* 9–11, 1981.

DESHPANDE, M. D. & GIDDENS, D. P. 1980 *J. Fluid Mech.* **97**, 65–89.

DI PRIMA, R. C. & SWINNEY, H. L. 1981 In *Topics in Applied Physics*, vol. 45 (ed. H. L. Swinney & J. P. Gollub), pp. 139–180. Springer.

EATON, J. K. & JOHNSTON, J. P. 1981 *AIAA J.* **19**, 1093–1100.

EATON, J. K., JOHNSTON, J. P. & JEANS, A. H. 1979 *2nd Symp. on Turbulent Shear Flows, Imp. Coll. London, July 2–4, 1979.*

ELENA, M. 1977 Etude des structures dynamiques et thermiques d'un écoulement turbulent en conduite avec aspiration à la paroi. Thèse Doct. Es. Sc. Phys. University Aix-Marseille, France, and *rapport CEA 1977* R. 4843.

Fulachier, L. 1972 Contribution à l'etude des analogies des champs dynamique et thermique dans une couche limite turbulente. Effet de l'aspiration. Thèse Doct. Es. Sc. Phys. Univ. de Provence, France.

Gent, P. R. & Taylor, P. A. 1976 *J. Fluid Mech* **77**, 105–128.

Gosman, A. D., Khalil, E. E. & Whitelaw, J. H. 1977 *Proc. Symp. on Turbulent Shear Flows. Univ. Park, Pennsylvania, April 18–20, 1977*, pp. 13–35.

Hanratty, T. J., Abrams, J. & Frederick, K. A. 1983 *I.U.T.A.M. Symp. on Structure of complex turbulent shear flow, Marseille, France*, (ed. R. Dumas & L. Fulachier). Springer.

Hinze, J. O. 1975 *Turbulence* (2nd edn) McGraw Hill.

Hsu, T. S. & Kennedy, J. F., 1971, *J. Fluid mech.* **47**, 481–502.

Hunt, I. A. & Joubert, P. N. 1979 *J. Fluid Mech.* **91**, 633–659.

Jackson, P. S. & Hunt, J. C. R. 1975 *Q. J. R. Met. Soc.* **101**, 929–955.

Jones, W. P. & Launder, B. E. 1972 *Intl J. Heat Mass Transfer* **15**, 301–313.

Jones, W. P. & Launder, B. E. 1973 *Intl J. Heat Mass Transfer* **16**, 1119–1129.

Kantorovich, L. V. & Krylov, V. I. 1964 *Approximate Methods of Higher Analysis*. Interscience.

Khabakpasheva, E. M., Yefimenko, G. N. & Gruzdeva, I. M. 1978 *Fluid Mech. Soviet Res.* **7**, 37–61.

Kuehn, D. M. 1980 *AIAA. J.* **18**, 343–344.

Laufer, J., 1954 *NACA Rep.* 1174.

Launder, B. E. 1975 *I.V.K. Lect. Ser. 76 on Prediction methods for turbulent flows.*

Lee, J. S. & Fung, Y. C. 1970 *Trans. ASME* E: *J. Appl. Mech.* **37**, 9–16.

McDonald, H. 1969 *J. Fluid Mech.* **35**, 311–336.

McLean, J. W. 1983 *Phys. Fluids* **26**, 2065–2073.

Macagno, E. O. & Hung, T. K. 1967 *J. Fluid Mech.* **28**, 43–64.

Markatos, N. C. G. 1978 *Comput. Meth in Appl. Mech. and Engng* **14**, 323–376.

Mellor, G. L. 1966 *J. Fluid Mech.* **24**, 255–274.

Mueller, T. J., Korst, H. H. & Chow, W. L. 1964 *Trans. ASME* D: *J. Basic Engng* **86**, 221–226.

Nikuradse, J. 1929 quoted in Goldstein, S., vol. ii, Clarendon Press, 1957.

Oberkampf, W. L. & Goh, S. C. 1974 In *Proc. Intl Conf. on Comput. Meth. in Nonlinear Mechanics, Austin, Sept. 1974*, pp. 569–579.

Okwuobi, P. A. C. & Azad, R. S. 1973 *J. Fluid Mech.* **57**, 603–622.

Patankar, S. V. 1980 *Numerical Heat Transfer and Fluid Flow*. Hemisphere.

Perry, A. E. & Fairlie, B. O. 1975 *J. Fluid Mech.* **69**, 657–672.

Pun, W. M. & Spalding, D. B. 1977 *Imp. Coll. HTS Rep.* 76/2.

Rodi, W. & Scheuerer, G. 1983 *Fourth Symp. on Turbulent Shear Flows, Karlsruhe, F. R. Germany.*

Schiestel, R. 1979 In *Rapport CEA/IMST*, *Contrat SA* 8323 and *Not. Interne I.M.S.T.*

Schiestel, R. & Chauve, M. P. 1982 *Intl J. Heat Mass Transfer* **25**, 1895–1904.

Smits, A. J., Baskaran, V. & Joubert, P. N. 1981 *Third Symp. on Turbulent Shear Flows, University of California Davis, Sept.* 9–11, 1981.

So, R. M. C. 1975 *J. Fluid Mech.* **70**, 37–57.

So, R. M. C. & Mellor, G. L. 1973 *J. Fluid Mech.* **60**, 43–62.

Spalding, D. B. 1961 *Trans. ASME* E: *J. Appl. Mech.* **28**, 455–458.

Sykes, R. I. 1980 *J. Fluid Mech.* **101**, 647–670.

Taylor, P. A., Gent, P. R. & Keen, J. M. 1976 *Geophys. J. R. Astr. Soc.* **44**, 177–201.

Thorsness, C. B., Morrisroe, P. E. & Hanratty, T. J. 1978 *Chem. Engng Sci.* **33**, 579–592.

Tritton, D. J. & Davies, P. A. 1981 *Topics in Appl. Phys.* (Ed. H. L. Swinney & J. P. Gollub), vol. 45, pp. 229–270. Springer.

Verdier, A. 1977 Ecoulement en régime lisse et rugueux avec aspiration pariétale à l'interieur d'un tube. Thèse Doct. Ing. University of Aix-Marseille II, France, *Rapport C.E.A.*, R. 4890.

Zilker, D. P., Cook, G. W. & Hanratty, T. J. 1977 *J. Fluid Mech.* **82**, 29–51.

Zilker, D. P. & Hanratty, T. J. 1979 *J. Fluid Mech.* **90**, 257–271.